Minimum size for the top jet drop from a bursting bubble

C. Frederik Brasz, Casey T. Bartlett, Peter L. L. Walls, Elena G. Flynn, Yingxian Estella Yu, and James C. Bird

A minimum size for the top jet drop from a bursting bubble

C. Frederik Brasz,[*] Casey T. Bartlett, Peter L. L. Walls,

Elena G. Flynn, Yingxian Estella Yu, and James C. Bird[†]

Department of Mechanical Engineering, Boston University, Boston, MA 02215

(Dated: June 25, 2018)

Jet drops ejected from bursting bubbles are ubiquitous, transporting aromatics from sparkling beverages, pathogens from contaminated water sources, and sea salts and organic species from the ocean surface to the atmosphere. In all of these processes, the smallest drops are noteworthy because their slow settling velocities allow them to persist longer and travel further than large drops, provided they escape the viscous sublayer. Yet it is unclear what sets the limit to how small these jet drops can become. Here we directly observe microscale jet drop formation and demonstrate that the smallest jet drops are not produced by the smallest jet drop-producing bubbles, as first predicted numerically by Duchemin et al. [Phys. Fluids, 14(9):3000 (2002)]. Through a combination of high-speed imaging and numerical simulation, we show that the minimum jet drop size is set by an interplay of viscous and inertial-capillary forces both prior and subsequent to the jet formation. Based on the observation of self-similar jet growth, the jet drop size is decomposed into a shape factor and a jet growth time to rationalize the non-monotonic relationship of drop size to bubble size. These findings provide constraints on submicron aerosol production from jet drops in the ocean.

I. INTRODUCTION

When a bubble at an air-liquid interface bursts, drops can be ejected by a liquid jet that forms at the base of the bubble [Fig. 1(a)]. Bubbles generated from breaking waves in the oceans produce these jet drops of salt water in abundance, carrying billions of tons of sea salt to the atmosphere every year [1]. These sea spray aerosol particles play an important role in climate, acting as cloud condensation nuclei and scattering radiation [2]. Aerosols from bursting bubbles have also been implicated in the transfer of pathogens [3] from the surf zone of coastal regions [4] and raindrops on soil [5], as well as on a smaller scale from recreational aquatic facilities [6] and toilets [7].

A key parameter in predicting the transport and residence time of an aerosol droplet is its size; larger drops quickly fall back to the surface, while microscopic drops are more easily lifted by turbulent eddies. Additionally, pathogen-laden drops smaller than $10\,\mu\text{m}$ in diameter can penetrate further into the respiratory tract than larger drops and therefore pose a higher risk for infection [8]. Over sixty years of experimental studies [9–24] have found that the radius of the top jet drop r_d is roughly 10% of the radius R of the bubble that produced it [Fig. 1(b)]. Yet, there is a scarcity of data to link smaller jet drops to the bubbles that produce them, and it is unclear how small these jet drops can be.

Many sea spray aerosol studies focus on particle sizes between 10 nm and $1\,\mu\text{m}$ [2, 25], as these dominate the production flux and are measurable using a scanning particle mobility sizer. These submicron aerosol particles are most often attributed to the breakup of films from larger bubbles (film drops), yet there is evidence that a significant fraction of these particles are formed by jet drops [26]. Because submicron jet drop particles have a different composition and stronger ice nucleating ability than film drop particles [26], climate and chemical transport models could be strengthened by understanding under what conditions submicron jet drops are formed and whether their size is bound by viscous effects.

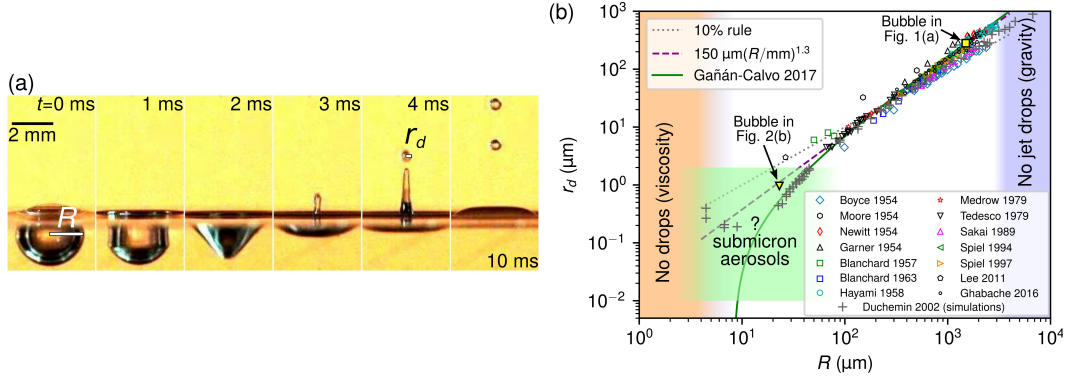[*] cfbrasz@gmail.com

[†] jbird@bu.edu

FIG. 1. Jet drops produced from a bursting bubble. (a) An air bubble of radius $R = 1.5$ mm at an air–water interface produces a jet drop of radius $r_d = 280\,\mu$m within time $t = 4$ ms after rupturing. (b) Decades of experiments (open symbols), most gathered in Lewis & Schwartz [2], have related the size of the top jet drop r_d to the bubble size R in fresh and salt water at various temperatures [9, 11–24]; yet these measurements fall outside the regime in which submicron aerosols from these jet drops might be expected (green shaded box). Results from a computational study [27], included as plusses and dimensionalized to seawater at 20 °C, suggest a non-monotonic dependence of r_d on R in this region. Also plotted are two data points from this study (yellow filled symbols), the smaller of which extends into the submicron regime and has properties similar to salt water at 8 °C. The commonly assumed "10% rule" (dotted line), an empirical power law dependence [2] $r_d = 150\,\mu$m$(R/$mm$)^{1.3}$ (dashed line), and a theoretical scaling relationship [28] for 20 °C seawater (solid curve) are included, along with regions where no jet drops are expected as a result of either viscous or gravitational effects.

It has been suggested that viscous effects prevent ocean bubbles smaller than $R = 4\,\mu$m from producing jet drops [23]. If the commonly assumed "10% rule" were applied, the minimum jet drop size would be $r_d = 400$ nm. Other empirical power laws of the form $r_d \sim R^p$ have been proposed [2, 15, 18, 21, 22, 24] with p ranging from 1.2 to 1.5, and these would produce different minima if they were extrapolated to this viscous cutoff. However, a numerical study [27] and recent theoretical scaling analysis [28] suggest a singularity before or at the viscous cutoff, allowing for jet drops to get arbitrarily small and likely regulated by a different mechanism. Here we investigate the mechanism that sets the minimum jet drop size by directly visualizing the formation of micron-scale jet drops. Figure 1(b) highlights that while the various models are consistent with available experimental data, they diverge in the region where data is scarce, which is precisely the region that is relevant to submicron jet drop aerosols. We combine dynamic similitude and numerical simulations to obtain and rationalize the bubble–jet drop size dependence at the smallest scales, and we explore the implications for submicron aerosol production in the oceans.

II. DYNAMIC SIMILITUDE FOR THE SMALLEST JET DROPS

With decreasing bubble and jet drop sizes, imaging becomes increasingly difficult for two reasons. First, spatially resolving the jet drops requires higher magnification and more precise alignment of the bubble before it ruptures. Second, temporally resolving the jet drops requires faster frame rates and shorter exposure times, because the jetting dynamics scale with the inertial-capillary timescale $\tau = \sqrt{\rho R^3/\gamma}$, where ρ is the liquid density and γ is the surface tension. In response to these challenges, we fabricate microfluidic devices with PDMS-soft-lithography that allow us to repeatedly

create and observe the spontaneous rupture of microbubbles of air with an inverted microscope and high-speed camera (see Appendix A, Fig. 5, and Movies 1–2 in the Supplementary Material [29]). Air bubbles within the device range in size from $R = 20 - 40\,\mu m$ and create discernible jet drops with radii r_d between 1 and $4\,\mu m$ within $30\,\mu s$ following rupture [Figs. 2(a)-(b)]. These jet drops appear to be the smallest reported from direct measurements for any liquid [Fig. 1(b)]; yet they do not rule out the possibility that even smaller jet drops would be generated from smaller bubbles.

To investigate the smallest top jet drops possible for a given liquid, we exploit dynamic similitude within the microfluidic device. Surface tension and inertia dominate jet drop dynamics and set the characteristic timescale τ. Viscous and gravitational effects can also be significant [23, 24, 27, 30, 31], especially if the bubble size approaches their characteristic lengthscales, $R_\mu \equiv \mu^2/\rho\gamma$ and $R_g \equiv \sqrt{\gamma/\rho g}$ respectively, where μ is the liquid viscosity and g is the acceleration due to gravity. For example, when $R \lesssim 370 R_\mu$, viscosity inhibits jet drop formation [23]; whereas if $R \gtrsim R_g$, gravity inhibits jet drop formation [30, 31] [shaded regions in Fig. 1(b)]. Therefore, jet drop dynamics can be recast in terms of two independent dimensionless groups, which we select as the Laplace number $\mathrm{La} \equiv \rho\gamma R/\mu^2 = R/R_\mu$ and the Bond number $\mathrm{Bo} \equiv \rho g R^2/\gamma = (R/R_g)^2$. We have chosen the Laplace number rather than the more common Ohnesorge number $\mathrm{Oh} \equiv 1/\sqrt{\mathrm{La}}$ because the Laplace number scales linearly with the size of the bubble. Note that we anticipate gravity has a negligible influence on the size of jet drops from microbubbles and, as a consequence, the size ratio r_d/R depends predominantly on the Laplace number.

We vary the Laplace number within the microfluidic device by working with glycerol-water solutions of varying concentrations [Table I], allowing us to elucidate the role of viscous effects on the size of the top jet drop. Figure 2(b) depicts the bubble and first discernible jet drop for three different Laplace numbers by displaying the intensity difference for images before and after each bubble ruptures; specifically, the subtracted image is dark where the source images differ and light where they are similar, with a pixel intensity given by 255 (white) minus the absolute value of the difference between images. As expected, the bubble with $\mathrm{La} < 370$ does not produce jet drops, a result consistent with past experiments [23] and simulations [31]. Yet as the Laplace number decreases toward this threshold, the results suggest that the ratio between the radii of the top jet drop and the bubble r_d/R increases, contrary to the behavior for larger bubbles [Fig. 1(b)].

To increase the spatial resolution and confirm the results extend beyond the microfluidic platform, we conduct experiments in which larger bubbles ($R \approx 200\,\mu m$) rise from the tip of a pulled glass micropipette and rupture at a free interface [Fig. 6]. Provided that the Bond number is less than $\mathrm{Bo} \approx 0.01$, gravity negligibly distorts the bubble shape [31]; this condition is met when $R < 300\,\mu m$ in glycerol-water mixtures. Figure 2(d) shows snapshots of the jet shortly after pinch-off for a range of glycerol-water solutions (see also Movie 3 [29]). A non-monotonic dependence of jet drop size on viscosity, or equivalently Laplace number, is evident. Jet drop size initially decreases with Laplace number, reaching a minimum of $r_d = 5\,\mu m$ ($r_d/R = 0.025$) at $\mathrm{La} = 1000$. Below this Laplace number, the ratio of jet drop to bubble size increases until jet drops are no longer ejected for $\mathrm{La} < 320$, similar to the trend from microfluidic experiments [Fig. 2(b)]. This non-monotonic relationship was first observed in the numerical simulations of Duchemin et al. [27] [Fig. 1(b)], which also found a minimum drop size between $\mathrm{La} = 600$ and $\mathrm{La} = 1500$. However, subsequent empirical and theoretical models of jet drop size [2, 24, 28] [Fig. 1(b)] have largely ignored this predicted non-monotonic behavior. Furthermore, the simulations of Duchemin et al. [27] had limited resolution and sparse results near the minimum jet drop size and, combined with our experiments, do not rule out the possibility that even smaller jet drops can be formed.

Given the limits of the experimental data and previous simulations, we carry out new jet drop simulations with significantly increased resolution, neglecting gravity to isolate viscous effects. We simulate bubble collapse and jet drop formation with the open-source computational fluid dynamics solver Gerris [32–34], which solves the incompressible Navier-Stokes equations with a fractional-step projection method, using an adaptive quad/octree spatial discretization and a multilevel Poisson
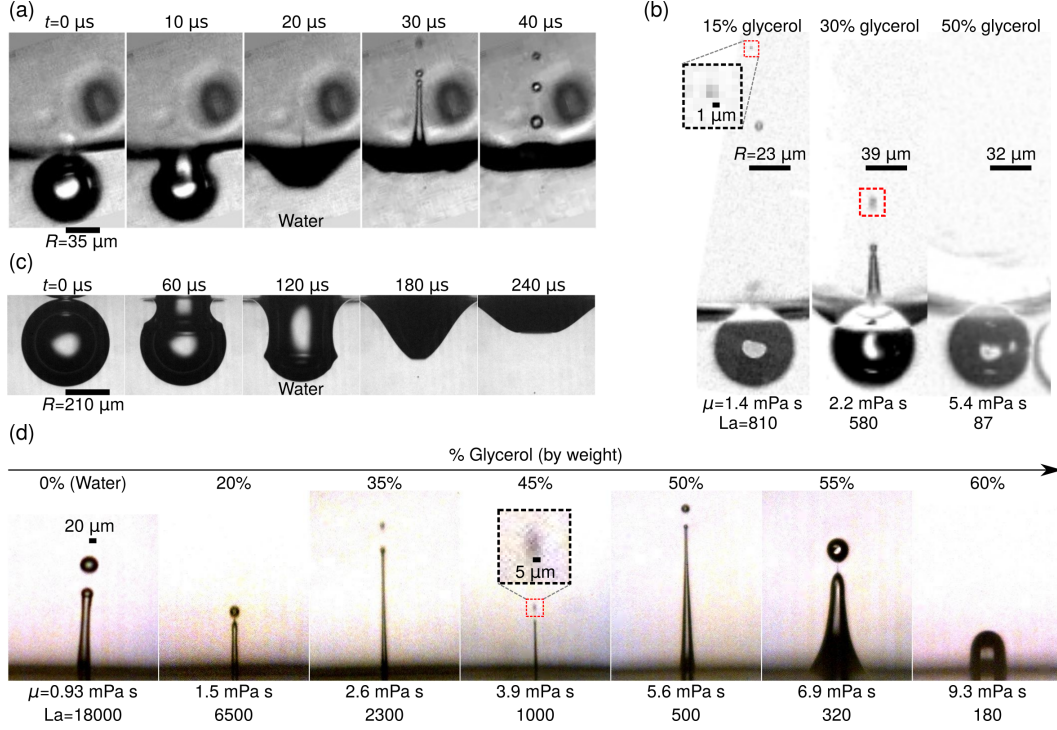
FIG. 2. Experimental images of bursting bubbles and resulting jet drops. (a) A microfluidic device provides a precisely designed environment to directly observe jet drops from the rupture of a microbubble. (b) Replacing the surrounding liquid with glycerol-water solutions of varying concentrations primarily changes the viscosity μ and therefore the Laplace number $\mathrm{La} \equiv \rho\gamma R/\mu^2$. Changing the Laplace number within the microfluidic device changes the jet drop size, illustrated here by image subtraction for times before and after rupture. The dashed boxes highlight the first discernible jet drop. (c) Micropipette experiments reveal finer detail of the bubble-bursting process by generating bubbles of radius $R \approx 200\,\mu\mathrm{m}$ that collapse within hundreds of microseconds. Note that the initial bubble shape in both microfluidic and micropipette experiments is nearly spherical. (d) Changing the glycerol concentration of the liquid in the micropipette experiments reveals a non-monotonic relationship between the Laplace number and the size of the first discernible jet drop. No jet drops are formed for $\mathrm{La} < 320$.

solver. A volume of fluid (VOF) scheme is used to capture the air-liquid interface, and its accurate, well-balanced surface tension model has led to its use for many interfacial flow problems [33–36]

We initialize the bubble with a small hole to approximate rupture (see Appendix B for more details on simulation setup) and evolve this shape in time for a range of Laplace numbers. Snapshots [Fig. 3(a) and Movie 4 [29]] reveal how capillary waves originating from the retreating rim focus at the bottom of the cavity, inverting it at time t_0 into a jet that pinches off its first jet drop at time t_p. The non-monotonic relationship between Laplace number and drop size mirrors that seen in our experiments [Fig. 2(b)]. The ratio of jet drop size to bubble size again reaches a minimum at $\mathrm{La} = 1000$, now of $r_d/R = 0.008$, and the critical Laplace number below which no drops are ejected is found to be $\mathrm{La}_c = 430$. We note that a recent numerical and experimental investigation of the velocities of jets from bursting bubbles reported $\mathrm{La}_c = 500$ and also found that an optimum Laplace number around $\mathrm{La} = 1000$ leads to the fastest jets when gravity is negligible [36].

The combination of experiments and high-resolution simulations provides evidence that the jet
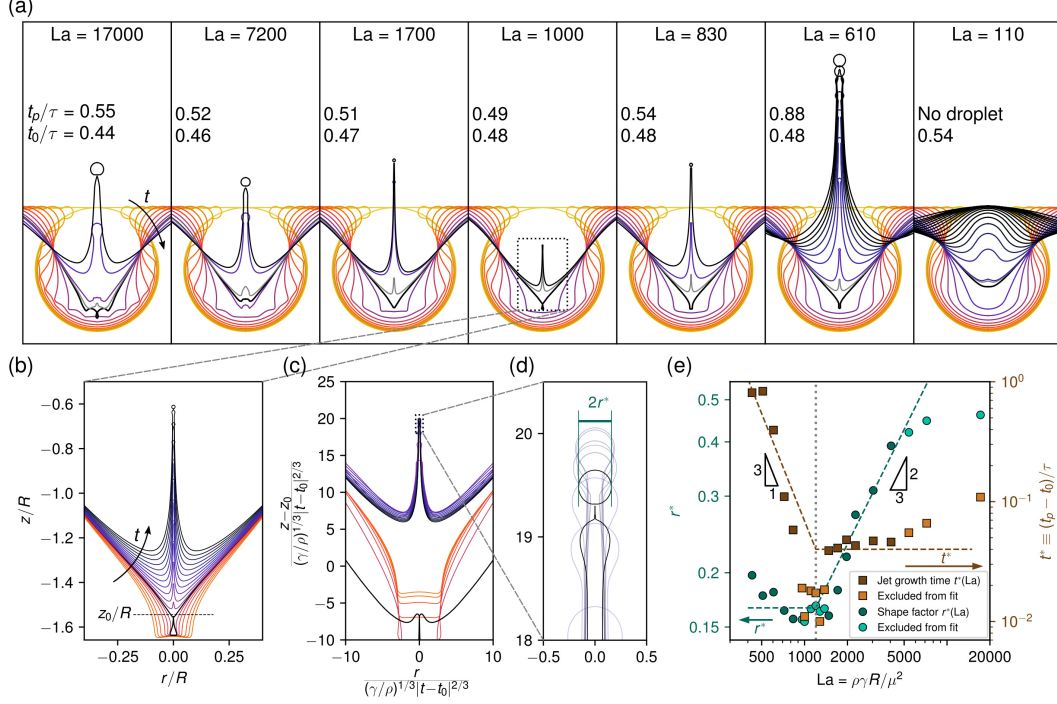
(a)

FIG. 3. Simulations of jet drops forming from bursting bubbles. (a) Superimposed profiles spanning the formation of the top jet drop demonstrate the non-monotonic dependence of jet drop size on Laplace number La. Pinch-off times and inversion times are labelled as t_p and t_0, respectively, and scaled by the inertial-capillary time $\tau = \sqrt{\rho R^3/\gamma}$. The time between successive interfaces is 0.05τ, with the exception of black curves at t_0 and t_p and a gray curve at $t_0 + 0.005\tau$. (b) Close-up view of final stages of cavity collapse, inversion, and jet growth until pinch-off for La = 1000, with the time between interfaces scaling as $|t - t_0|^{3/2}$ and spanning $0.471 \leq t/\tau \leq 0.486$. The base of the jet at inversion is labelled as z_0/R. (c) A self-similar scaling of the same profiles shows an approximate collapse of the growing jet. (d) Close-up of the tip of the jet in self-similar coordinates, with the diameter labelled as $2r^*$. (e) The shape factor $r^* \equiv r_d(\rho/\gamma)^{1/3}(t_p - t_0)^{-2/3}$ and jet growth time $t^* \equiv (t_p - t_0)/\tau$ extracted from simulations of varying Laplace number. Both relationships are approximated by "hockey stick" fits, shown as dashed lines. Symbols with lighter shade denote data points excluded from the fits (see Appendix C).

drops observed in the experiments are indeed the top jet drops and that there are no smaller, undetected drops emitted earlier in the jetting process. Specifically, our numerical results are sufficiently resolved to establish that the top drop from a bubble of radius $R = 200\,\mu$m for La = 1000 is larger than $1.5\,\mu$m in radius. Even with significant variability in jet drop size for nearby Laplace numbers (discussed further below), additional simulations find a minimum of $r_d/R = 0.0057$, corresponding to $r_d = 1.1\,\mu$m. The drop diameters are larger than our experimental resolution of $1.3\,\mu$m/pixel, and therefore we conclude that our experimental setup has the optical resolution to detect the smallest top jet drops. To determine what sets the size and differences between the experiments and simulations, we explore the underlying mechanisms.

III.   ORIGINS OF MINIMUM DROP SIZE AND NON-MONOTONIC BEHAVIOR

Taken together, the experiments and numerical simulations illustrate that viscous stresses alone can lead to a non-monotonic relationship between the ratio of top jet drop radius to bubble radius r_d/R and the Laplace number, as first suggested by the numerical simulations of Duchemin et al. [27]. Fundamentally, this non-monotonic relationship is interesting because it suggests that viscous stresses can both decrease and increase the jet drop size relative to the bubble. Duchemin et al. [27] speculated that this relationship might originate from a cusp singularity set up by bubble entrapment; yet, they also note that bubble entrapment is numerically observed for other Laplace numbers where the singularity is not. By contrast, we propose that the non-monotonic behavior is primarily the result of two separate mechanisms: one that occurs during the collapse of the bubble, and another that occurs during the pinch-off of the jet drop. During the collapse of the bubble, viscous stresses dampen capillary waves and lead the cavity to adopt a self-similar profile [27, 37]; that is, the influence of the external length scale R disappears as the cavity collapses and is replaced with a characteristic length scale $(\gamma/\rho)^{1/3}(t_0 - t)^{2/3}$, where t_0 is the singular time when the cavity inverts to form a jet. Increased dampening of these waves allows for greater self-similar focusing of cavities, narrower resulting jets [36, 37], and by extension smaller jet drops [24]. Meanwhile, increasing viscous stresses can increase the time it takes for a liquid jet to break up into droplets [35, 38]. Therefore, as a second mechanism, we propose that the far-field dynamics that lead to a self-similar collapsing cavity before inversion also lead to a self-similar upward jet after inversion, and thus a delay in pinch-off from viscous stresses enlarges the top jet drop. While the self-similarity of collapsing cavities from bubbles [27, 37] and over-driven Faraday waves [39] is well-established, the authors are aware of only one study suggesting the self-similarity of growing jets, for the case of cavity collapse following drop impact on a hydrophobic surface [40].

To determine whether the jet shape exhibits self-similarity following bubble collapse, we consider the simulations for $\mathrm{La} = 1000$ and enlarge the interface profiles that span from slightly before inversion through pinch-off [Fig. 3(b)]. Note that the negative values of height z signify that the jet is below the initial free surface. By referencing the height with respect to the base of the jet at inversion z_0 and re-scaling both the axial and radial axes by the self-similar length scale, the profiles in Fig. 3(b) collapse predominantly onto one of two master curves [Fig. 3(c)]: one corresponding to the self-similar shape of the cavity and the other to the jet. A closer inspection of the jet tip in scaled coordinates reveals that the tip radii of these overlaid profiles collapse fairly well [Fig. 3(d)], supporting the hypothesis that the shape of the jet is approximately self-similar through pinch-off. A more thorough analysis of the self-similarity of jets after inversion is presented in Appendix C and Figs. 10–11, finding that several length scales associated with the jet grow approximately as $(t - t_0)^{2/3}$ for simulations with a range of Laplace numbers, as predicted for this inertial-capillary self-similarity. We note that a pair of papers [41, 42] investigating the generation and breakup of Worthington jets following cavity collapse defined lengths of a growing jet in a similar way (see Fig. 14 in Gekle & Gordillo 2010 [41]); they ignored viscous effects and did not test for self-similarity, however.

The observation of self-similar jet growth motivates the decomposition of the jet drop size into two components: one due to the time for which the jet grows before pinching off, defined as $t^* \equiv (t_p - t_0)/\tau$; and another that depends only on the shape of the cavity at inversion and the subsequent self-similar jet shape, independent of jet growth time. A convenient choice for this shape factor is the self-similar radius of the jet drop at pinch-off $r^* \equiv r_d(\rho/\gamma)^{1/3}(t_p - t_0)^{-2/3}$, allowing us to write $r_d/R = r^*(\mathrm{La})\,(t^*(\mathrm{La}))^{2/3}$. Both r^* and t^* are plotted against La in Fig. 3(e), and the general trends of both factors are captured by the piecewise power-law fits $r^*(\mathrm{La}) = 0.166\max\big(1, (\mathrm{La}/1200)^{0.66}\big)$ and $t^*(\mathrm{La}) = 0.040\max\big((\mathrm{La}/1200)^{-3}, 1\big)$. These "hockey-stick" fits suggest that for $\mathrm{La} \lesssim 1200$, jets grow self-similarly with a nearly constant shape factor r^*, and most of the variation in jet drop size

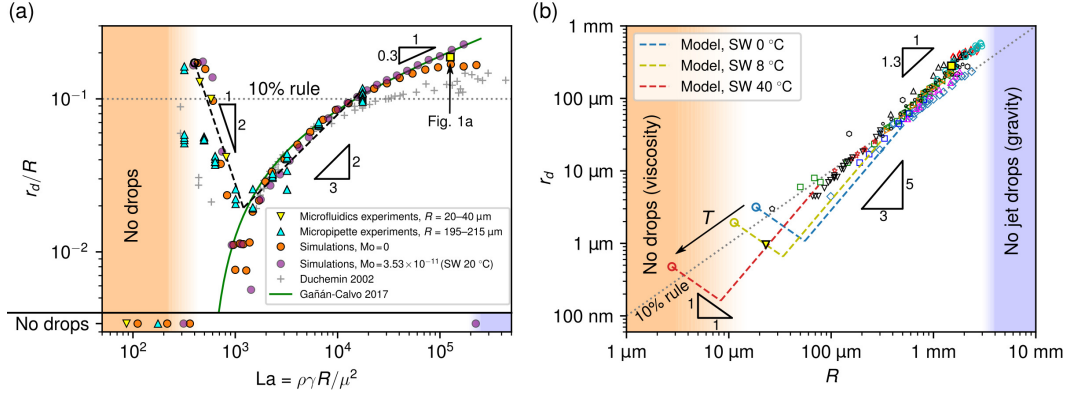

FIG. 4. Dimensionless and dimensional plots of jet drop radius relative to bubble radius. (a) Ratio of jet drop radius to bubble radius as a function of Laplace number for both sets of experiments and simulations. The dashed black line corresponds to Eq. (1), the self-similar model prediction based on Fig. 3(e). The solid green curve denotes the theoretical scaling [28] $r_d/R = k_d(\sqrt{\mathrm{La}/\mathrm{La}_c} - 1)^{5/4}/\mathrm{La}^{3/8}$, with $k_d = 0.6$ and $\mathrm{La}_c = 540$. (b) Jet drop radius as a function of bubble radius from previous studies [same symbols as Fig. 1(b)], along with the re-dimensionalized model, Eq. (2), for seawater at temperatures of $0\,^\circ$C, $8\,^\circ$C, and $40\,^\circ$C. The yellow triangle corresponds to the microfluidic data point [Fig. 2(b)] from the 15% glycerol-water solution, as the liquid properties are similar to seawater at $8\,^\circ$C.

can be attributed to jet growth time t^* increasing as La decreases [Fig. 10(b)]. For La $\gtrsim 1200$, the jet growth time is instead approximately constant, but the shape factor increases with La [Fig. 11(a)].

The two monotonic fits for r^* and t^* combine to produce a non-monotonic expression for the jet drop size ratio

$$r_d/R = 0.020 \max\left((\mathrm{La}/1200)^{-2}, (\mathrm{La}/1200)^{0.66}\right), \tag{1}$$

shown with dashed curves in Fig. 4(a) alongside measurements from experiments and simulations of the top jet drop radius. This model provides a useful estimate for r_d/R in the range $400 \lesssim \mathrm{La} \lesssim 10000$, capturing the non-monotonic trend between r_d/R and La from experiments and simulations. The model and experiments predict r_d/R reaching a minimum of 0.02, and simulations suggest it could reach as low as 0.006. Some of the size variability may be attributed to rapid re-coalescence of the top drop to subsequent drops as well as "escape from pinch-off" [35], a temporary reversal of the narrowing of the neck of a jet [Fig. 8]. In any case, we provide a floor for the ratio of jet drop radius to bubble radius at which the theoretical scaling [28] [green curve in Fig. 4(a)] breaks down. In addition, we provide evidence that viscous effects related to the pinch-off time of the jet are responsible for the minimum drop size. While it may seem counter-intuitive that the model uses inviscid self-similar scalings to predict the size of the ejected top drop, as the ejection process is a clear deviation from self-similar behavior, we emphasize that the self-similar growth is coupled with the Laplace number-dependent pinch-off time of the jet $t^*(\mathrm{La})$ to obtain an estimate for r_d/R. We also note that $r^*(\mathrm{La})$ can be fit with the same functional form as that of the theoretical scaling [28] for La $\gtrsim 1200$ to give a similar curve with slightly differing fitting coefficients.

Thus far, our analysis has assumed that gravitational effects are negligible, an assumption that breaks down for sufficiently large bubbles. To probe this transition, we run additional simulations that include the effects of gravity [purple symbols in Fig. 4(a)]. Gravity acts on the jet and drops as they form, but the more significant effect for jet drop formation was found [31] to be the change

in the equilibrium shape of the bubble before bursting [43, 44], shown for a few Bond numbers in Fig. 7. These simulations are conducted using bubbles of varying radius in seawater at 20 °C, for which $R_g = 2.7$ mm and $R_\mu = 16$ nm. A convenient dimensionless parameter to describe these simulations is the Morton number, $\mathrm{Mo} \equiv g\mu^4/\rho\gamma^3 = (R_\mu/R_g)^2$, which depends only on fluid properties and is $\mathrm{Mo} = 3.5 \times 10^{-11}$ here. In contrast, the simulations without gravity have a Morton number $\mathrm{Mo} = 0$. As expected, simulations with and without gravity show the same behavior at small Laplace numbers and only start to differ at the largest Laplace numbers; gravitational effects are indeed negligible when $\mathrm{Bo} \lesssim 0.01$, which corresponds to $\mathrm{La} \lesssim 17000$ for seawater at 20 °C. Interestingly, for large bubbles, the theoretical scaling [28] shows better agreement with our simulations including gravity than those neglecting it, despite gravity being ignored in the analysis. Although our analysis indicates that gravitational effects are not significant for the smallest jet drops over the ocean, they likely set the size of the smallest drops for more viscous liquids with higher Morton numbers, consistent with previous studies [24, 31, 36].

IV.   CONCLUSIONS AND IMPLICATIONS

The results in this study provide clarity on the conditions that lead to the smallest top jet drops from bursting bubbles. Specifically, we report systematic experiments on the jet drop size when gravitational effects are negligible. Together with high-resolution simulations, our experiments provide evidence that the minimum size for the top jet drop is approximately 1% of the size of the initial bubble. We attribute the minimum size to a confluence of two counteracting processes: viscous stresses before jet formation decrease drop size by sharpening a self-similar shape factor and viscous stresses after jet formation increase drop size by increasing the jet growth time. These competing processes provide a means by which the minimum drop size also depends on a balance of viscous and inertial-capillary stresses rather than depending on a singularity that is regulated by a separate set of dynamics.

To illustrate the implications of our study to sea spray aerosol production in the oceans, we convert the model to dimensional form by taking reference values for the viscosity, density, and surface tension of seawater [45, 46]. Of particular interest has been the role of temperature in modifying the jet drop size, as previous experiments have found contradictory results [12, 15, 16]. Over a temperature range of 0 °C to 40 °C, the density and surface tension of seawater vary by less than 5%, whereas the viscosity decreases by nearly a factor of three [Table S2]. Fitting the temperature dependence of the viscous length scale $R_\mu(T)$ for seawater [Fig. 12] and recalling that $\mathrm{La} = R/R_\mu$ allows us to manipulate equation (1) to obtain an expression for the drop radius as a function of bubble radius and temperature,

$$r_d(R, T) = 0.020R \max\left[(A(R, T))^{-2}, (A(R, T))^{0.66}\right], \qquad (2)$$

where

$$A(R, T) = 13.4 \, \exp\left(-\frac{661}{100 + T/°\mathrm{C}}\right) R/\mathrm{\mu m}. \qquad (3)$$

Note that the temperature changes both the Morton and Laplace numbers, but because of the bubble size, our analysis need only consider the contribution of the Laplace number. Equation (2) is plotted for two extreme ocean temperatures as well as $T = 8$ °C [Fig. 4(b)], a temperature at which seawater has a viscous length scale similar to the 15% glycerol-water solution [Fig. 2(b) and yellow triangle in Fig. 4(b)]. Bubbles of radius $R \approx 50 \, \mathrm{\mu m}$ are predicted to form jet drops of radius $r_d \approx 1.2 \, \mathrm{\mu m}$ in polar waters around 5 °C and at least twice that size in tropical waters around 30 °C. Meanwhile, smaller bubbles of radius $R \approx 10 \, \mathrm{\mu m}$ are predicted to produce jet drops with $r_d \approx 300$ nm in

tropical waters; whereas the drops would be larger in cooler temperate waters, and non-existent in polar waters. This size and temperature-dependent relationship may provide insight into why large ($>$ 1 μm) aerosol particle production increases with increasing temperatures while small aerosol particle production remains constant or decreases [47, 48]. Similarly, this relationship can be applied to pathogen transfer in a wide range of urban environments. Our findings suggest that the bubble sizes leading to effective transport of pathogens in jet drops would differ between a public drinking fountain (5 °C) and a hot tub (40 °C). More generally, our analysis elucidates the missing range of top jet drop sizes from microscopic bubbles [Fig. 1(b)] and constrains jet drops as a source of submicron aerosols. Although marine aerosols are observed at sizes less than 100 nanometers, our findings suggest that it is unlikely these smallest aerosols originate from top jet drops.

Appendix A: Experimental setup

A microfluidic device is fabricated from Polydimethylsiloxane (PDMS) and bonded to a glass microscope slide with the design shown in Fig. 5. Air and liquid are injected into the three labelled circular ports in Fig. 5(a) via syringe pump, with an inlet pressure of $P \approx 50$ kPa for the air. Channels direct the air and liquid to meet at the junction in Fig. 5(b), where they are forced through a nozzle of diameter 10 μm; the air repeatedly pinches off to form bubbles of repeatable size (20–40 μm). Additional liquid flows through a side channel after the nozzle, which increases the spacing between bubbles and prevents coalescence. Movie 1 shows these bubbles being produced at a rate of around 5000 bubbles per second [29]. The air bubbles are then carried in a channel of height and width 80 μm to the circular outlet port of the device [Fig. 5(c)]. Here, the bubbles encounter a large pocket of air at atmospheric pressure and burst, producing a liquid jet that breaks up into jet drops [Fig. 2(a) and Movie 2 [29]]. Images of the process are captured using a Zeiss A1 Axio Observer inverted microscope together with the Photron FASTCAM SA5 (described below).

Densities and surface tensions of glycerol-water solutions are obtained from reference values [49] assuming a temperature of 25 °C, and viscosities are obtained from an empirical formula [50] that accounts for temperature variations [Table I]. Lab temperatures varied from 21.5 °C to 25.5 °C.

For the micropipette experiments, glass micropipettes are made with a programmable micropipette puller and threaded through a rubber stopper into a glass test tube containing water or a glycerol-water solution. The micropipette is connected to a syringe pump and injects individual air bubbles into the liquid that rise to the surface and burst [Fig. 6(a)]. The bubble radius is found by imaging it upon release from the micropipette [Fig. 6(b)]. Bubble sizes from five micropipettes in solutions with varying glycerol concentrations were averaged to find the linear fit $R/\mu m = 212.5 - 23.2C$, where C is the mass fraction of glycerol in the solution, with a standard deviation of 18.1 μm or about 8.5%. Densities and surface tensions of glycerol-water solutions are again obtained from reference values [49], and viscosities are measured with a viscometer, agreeing with the formula from the literature [50] [Table I].

Experimental images are obtained with a Photron FASTCAM SA5 or SA-X2 at frame rates between 45000 and 100000 frames per second and shutter speeds between 300 ns and 1 μs. Jet drop and bubble radii are measured with ImageJ, with resolutions of 0.96 μm/px and 1.35 μm/px for microfluidic and micropipette experiments, respectively.
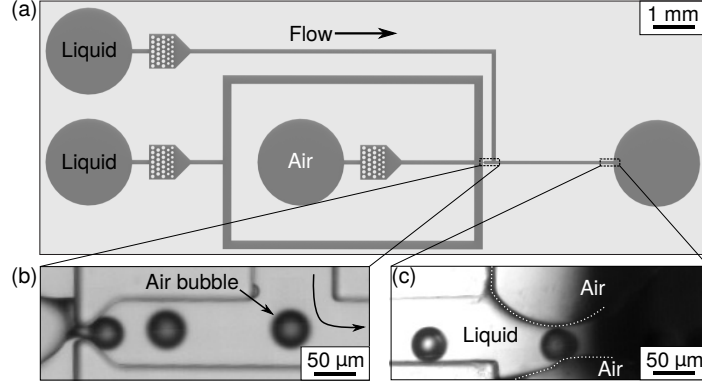
FIG. 5. Microfluidic device design. (a) Schematic of the microfluidic device with channel flow moving from left to right. Air and liquid enter channels through the three circular ports at the left hand side of the device. (b) The liquid and air are forced through a $10\,\mu$m-diameter nozzle where air bubbles are formed. Bubbles produced at the nozzle are of radius $R \approx 30\,\mu$m. The channel width and height after the nozzle are $80\,\mu$m. (c) Air bubbles come into contact with an air-liquid interface and burst at the device outlet.
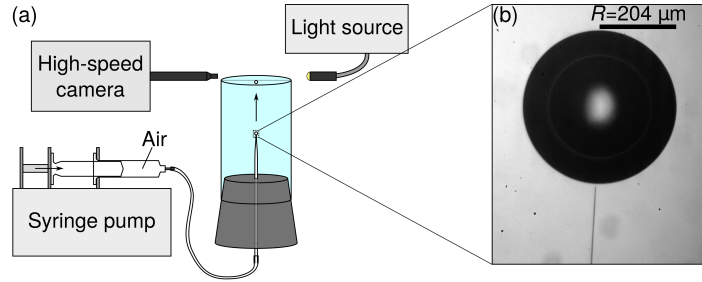

FIG. 6. Micropipette experimental setup. (a) Schematic of the micropipette experiment. (b) Image of an air bubble in a 20% glycerol-water solution just after pinching off from the micropipette.

Appendix B: Numerical simulations

We use the open-source package Gerris [32, 34] to solve the two-phase incompressible Navier-Stokes equations in an axisymmetric coordinate system with a volume-of-fluid method to capture the interface. The density and viscosity ratios correspond to water at 20 °C in air, with $\rho_g/\rho = 1.2 \times 10^{-3}$ and $\mu_g/\mu = 0.018$, where ρ_g and μ_g denote density and viscosity of the gas phase.

Simulations ignoring gravity are initialized as a spherical bubble resting at a flat gas-liquid interface with a hole to connect the bubble interior to the gas phase above the interface. This hole has a radius of $0.01R$, and the rim is a semicircular cap (in the axisymmetric domain). The computational domain is a cylinder of radius $4R$ and height $16R$, discretized as a 2D rectangle (four square "boxes" of side length $4R$) by using axisymmetry. The initially flat (apart from the hole connecting to the bubble) air-liquid interface $z = 0$ divides the domain in half. A free-slip, impermeable (symmetry) boundary condition is applied on the axis of symmetry $r = 0$ and $r = 4R$, while free outflow and inflow is applied at the top and bottom boundaries, $z = \pm 8R$, by enforcing a Dirichlet condition $p = 0$ for the pressure and Neumann condition $\partial v/\partial z = 0$ for the vertical velocity. The quadtree mesh is adaptively refined and coarsened based on the local vorticity and curvature of the interface to a maximum level of 14, which means that each box of length $4R$ can be subdivided up to 14 times,
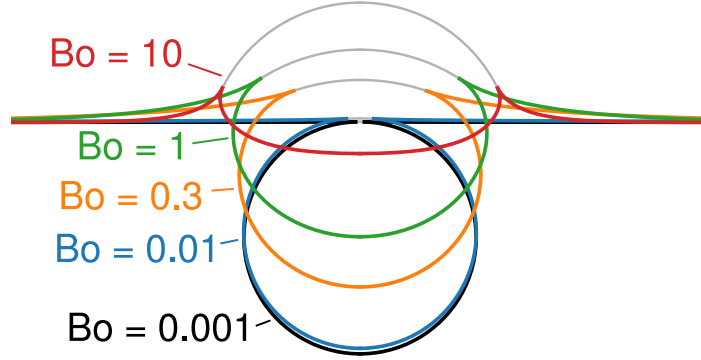
FIG. 7. Initial bubble shape for varying Bond number $\mathrm{Bo} = \rho g R^2 / \gamma$. Each bubble has a constant volume-equivalent radius R. For simulations including gravitational effects, the bubble is initialized without the spherical film cap (drawn in gray for each bubble).

resulting in a minimum cell size $\Delta = 4R/2^{14} = 2.4 \times 10^{-4} R$, or 4200 cells per bubble radius. This choice results in a radius of 31 cells for the top drop from the $\mathrm{La} = 1000$ simulation. Note that the maximum level of refinement based on vorticity is set to 10, so that only high-curvature regions of the interface achieve the maximum refinement.

For the simulations including gravity, the flattened equilibrium bubble shape and its deformation of the gas-liquid interface are calculated numerically as a function of Bond number with a shooting method, balancing hydrostatic and capillary pressures [43, 44]. The spherical thin film cap, which grows with Bond number, is removed entirely as an approximation of the initial rupture of the bubble. Figure 7 shows examples of the initial bubble shapes for a few Bond numbers, including their spherical caps. Note that the range of Bond numbers corresponding to the bubble radii tested was $3.5 \times 10^{-6} \leq \mathrm{Bo} \leq 1.8$. It is also worth emphasizing here that R is the volume-equivalent bubble radius, or $(3V/(4\pi))^{1/3}$ for bubble volume V. In some studies [31], the Bond number can refer to the radius of the spherical cap R_{cap}, which varies between $2R$ at small Bo and $2^{1/3}R$ at large Bo.

Interfaces are extracted for visualization and jet analysis purposes at a temporal resolution of 0.001τ, except for the simulations used to check self-similar scalings (discussed below and in Figs. 10–11), which used 0.0001τ near the inversion time for more accurate scaling. The actual timestep of the simulation is automatically set to ensure a CFL number $C \leq 0.8$ and typically varied between $10^{-7}\tau$ and $10^{-6}\tau$. The interface output from Gerris is a series of line segments in an arbitrary order, and a Python script is used to connect them to make a continuous interface curve. Bubbles formed during inversion are automatically removed to avoid occasional problems in running the solver, with small effects on jet drop size.

Simulations are run with a higher maximum level of refinement for 9 Laplace numbers between 720 and 7200 to check for grid independence. Comparing the base-level simulations to those with a higher maximum refinement level, inversion and pinch times vary by less than 0.5% and 4% respectively. Jet drop radius varies by up to 50% in the region ($960 \leq \mathrm{La} \leq 1300$) where r_d/R oscillates between large and small modes due to the uncertain escape from pinch-off process [Fig. 8], but the radii of these large and small modes are comparable to those from the normal simulations (around 2% variation). Outside of this region, jet drop radius differs by up to 7% between refinement levels. Figure 9 also shows good agreement between experiments and simulations for images of a collapsing bubble.
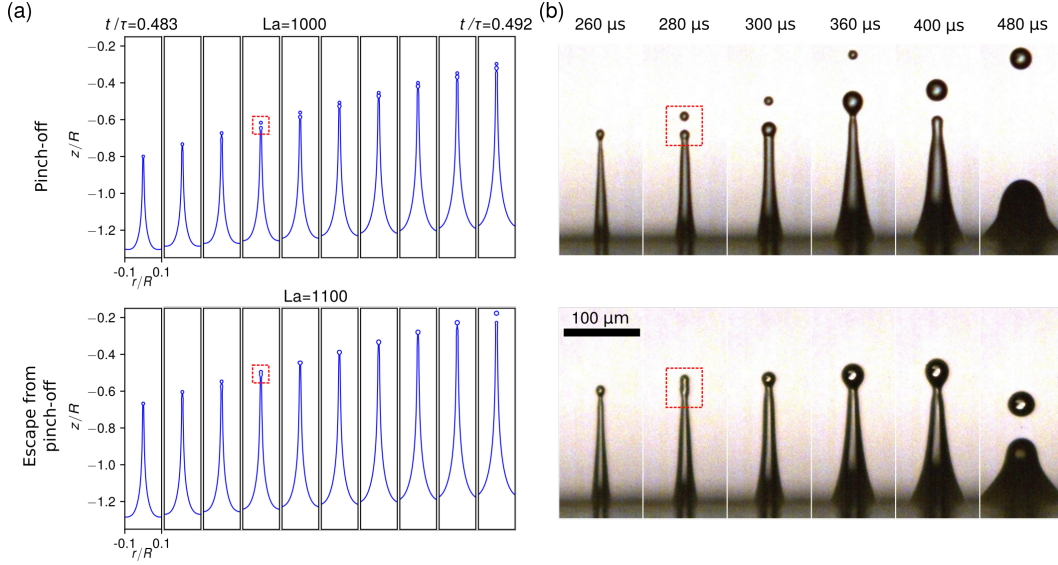
FIG. 8. Escape from pinch-off [35]. (a) For simulations near the minimum in jet drop size, in some cases the jet pinched off relatively early (La = 1000, top), while in others the jet initially escaped pinch-off (La = 1100, bottom). The neck radius temporarily reverses from shrinking to growing, and extra liquid is collected at the tip, resulting in a larger jet drop when it later pinches off. (b) Experiments with bursting bubbles of radius $R = 200\,\mu\text{m}$ in 55% glycerol solutions (La = 320) similarly had some jetting events with an early pinch-off (top) along with others in which the jet escaped pinch-off (bottom), leading to a much larger jet drop. Dashed boxes highlight the pinch-off and escape from pinch-off events in each case.

Appendix C: Self-similar scaling and fits

For the self-similar scaling, z_0 is defined as the height of the base of the jet at inversion, which we obtain by linearly extrapolating the base height half a timestep before the first timestep showing a jet (see also Fig. 10(a)). One could alternatively define z_0 as a limiting height of the cavity bottom in order to collapse the profiles of the cavity leading up to inversion, similar to previous studies [27, 37].

The "hockey stick" fits are obtained from least-squares linear fits of $\log r^*(\text{La})$ as a function of $\max(0, \log(\text{La}/1200))$ and $\log t^*(\text{La})$ as a function of $\min(\log(\text{La}/1200), 0)$. Zeroing out the Laplace numbers on either side of La = 1200 leads to a fit that is constant on one side and a power law on the other side, giving the hockey stick shape. The lighter symbols in Fig. 3(e) ($960 \leq \text{La} \leq 1380$ and $\text{La} \geq 5400$) were excluded from the fit to capture the general trend away from the much smaller drops near La = 1200 or the large Laplace numbers where the self-similarity assumption breaks down.

Figures 10 and 11 go into more depth on the validity of the self-similar jet growth hypothesis. First, Fig. 10(a) defines relevant length scales for the jet, including the initial base height at inversion z_0, the radius and height of the jet base r_b and z_b, the radius of the jet tip r_j, and the height of the jet z_j relative to the initial base height. The jet tip radius r_j is defined by obtaining all local maxima in the jet radius $r(z)$ and choosing the one with the largest value of z; note that there may be no maximum, especially early on in the jet formation process before surface tension forms the bulbous tip. In Fig. 10(b), these lengths are plotted versus dimensionless time past the inversion time for three simulations with La < 1200. Most of the jet lengths collapse well and approximately follow
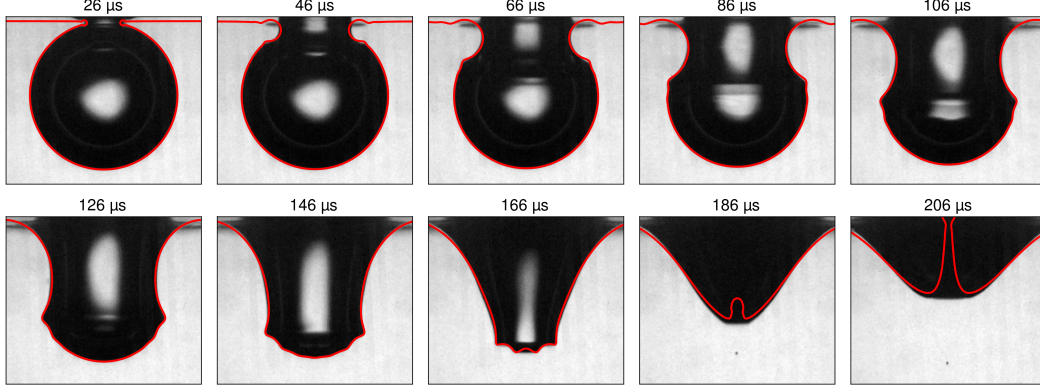
FIG. 9. Overlays of the air-water interface during bubble burst from simulation results (red) with experimental images. The experimental bubble radius is $R = 209\,\mu\text{m}$ and bursts in water, corresponding to a Laplace number La $= 17200$. The time between snapshots is $20\,\mu\text{s}$, and no fitting parameters are used other than the offset time, here $26\,\mu\text{s}$, of the first experimental image relative to $t = 0$ in the simulation.

the $(t - t_0)^{2/3}$ power law predicted for inertial-capillary self-similarity for a significant portion of the jet growth. Notably, the jet tip radius initially grows at a rate slower than $(t - t_0)^{2/3}$ in each simulation, but the final drop radii still lie along the model curve $r_d = 0.166(t_p - t_0)^{2/3}$. These scalings suggest that to a good approximation, the radius of the top jet drop in this La $\lesssim 1200$ regime is mainly controlled by the time for which the jet grows self-similarly before pinch-off, $t^* = (t_p - t_0)^{2/3}$.

Figure 11 considers the large-La regime, plotting the same lengths for three Laplace numbers with La > 1200. Jet tip and base radii [Fig. 11(a)] have been separated from jet and base heights [Fig. 11(b)] for clarity, as the lengths differ more between simulations. The jet tip and drop radii no longer lie along $0.166[(t - t_0)/\tau]^{2/3}$, as r^* varies approximately as $r^*(\text{La}) = 0.166(\text{La}/1200)^{0.66}$ in this regime. However, the hockey stick fits assume a constant jet growth time $t^* = (t_p - t_0)/\tau$ of 0.040, which is included as a vertical dotted line in Fig. 11(a) and agrees with the drop pinch-off times well for La $= 1700$ and 3000 but underpredicts t_p for La $= 7200$.

The base radius r_b deviates significantly from $(t - t_0)^{2/3}$ for La $= 3000$ and 7200 at early times due to a nonzero initial radius of the base resulting from capillary wave interference [Fig. 3(a)]. As the jet grows, however, the base radius does appear to approach an intermediate asymptotic regime where all three simulations collapse to the same curve proportional to $(t - t_0)^{2/3}$. The heights of the jet tips appear to grow with a power slightly larger than $2/3$, and the base height for La $= 7200$ follows $z_b/R \sim (t - t_0)/\tau$ at early times. Perhaps this relationship could be explained together with the constant base radius observed.
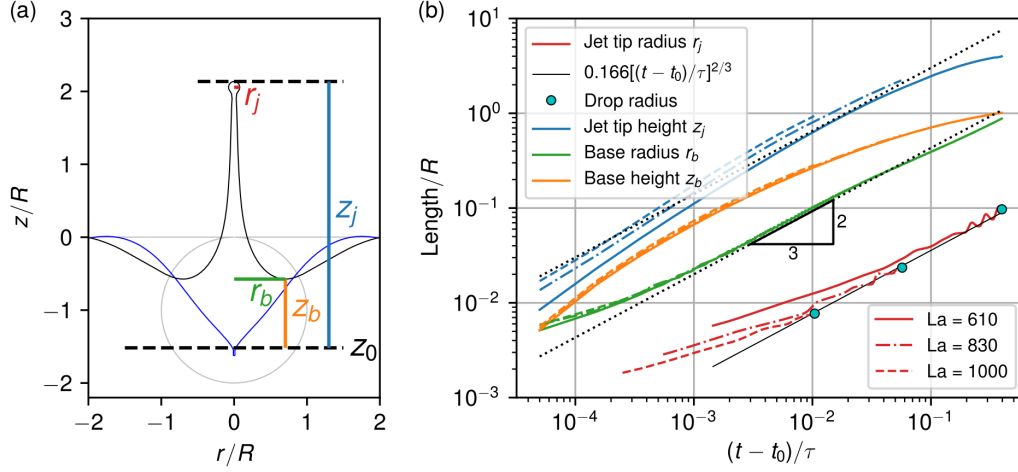
FIG. 10. Scaling of jet lengths after inversion for La < 1200. (a) Snapshot of jet at $t/\tau = 0.76$ for La = 610 with jet radius r_j, jet height z_j, base radius r_b, base height z_b, and base height at inversion z_0 labelled accordingly (omitting nondimensionalizing factors of R). The profiles at $t = 0$ and the inversion time t_0 are plotted in gray and blue, respectively. (b) Scaling of these jet lengths with $(t - t_0)/\tau$ for simulations with La = 610, 830, and 1000. Top drop radii are plotted at time of pinch-off with circles, and the curve $0.166[(t - t_0)/\tau]^{2/3}$ is the model prediction for self-similar jet drop radius evolution for La $\lesssim$ 1200, as $r^* = 0.166$ here.
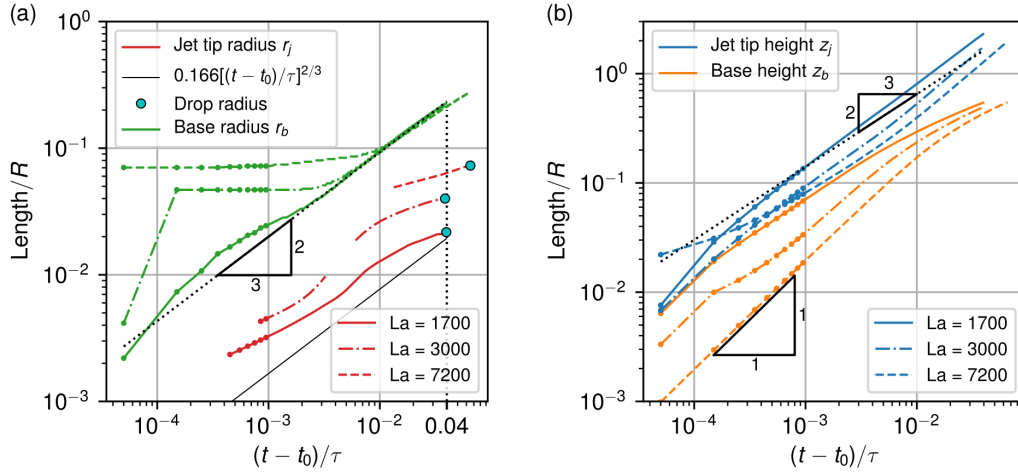

FIG. 11. Scaling of jet lengths after inversion for La > 1200. (a) In this regime, $0.166[(t - t_0)/\tau]^{2/3}$ is no longer a good estimate for jet tip or drop radius; the model instead assumes a constant scaled jet growth time to pinch-off of $t^* = 0.04$, shown here as a vertical dotted line. For larger Laplace numbers, the base radius starts at a nonzero value at inversion (as seen in Fig. 3(a)) but follows a $(t - t_0)^{2/3}$ scaling at later times. Markers have been added to the first 10 timesteps after inversion to highlight the temporal resolution of the data; the jump in r_b for La = 3000 is due to the inversion of a smaller jet base before the main one. (b) While the jet tip height z_j grows roughly with $(t - t_0)^{2/3}$, the base height z_b at large La appears to grow linearly with time.
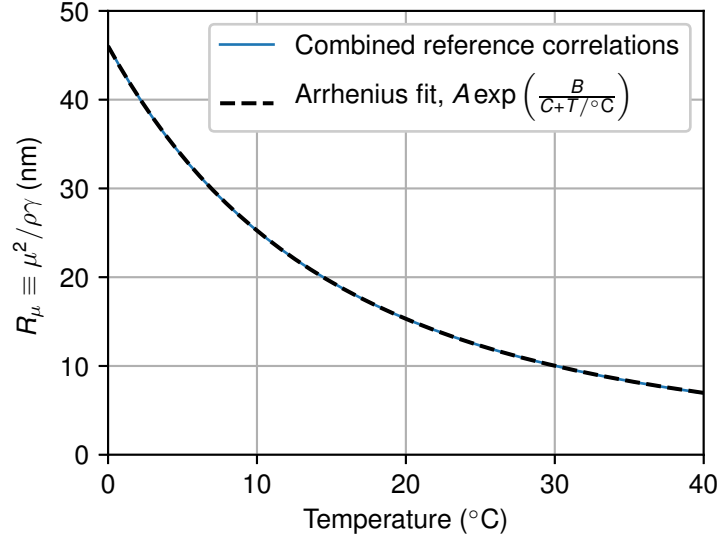
FIG. 12. Viscous length scale of seawater as a function of temperature. Reference correlations [45, 46] for the viscosity, density, and surface tension of seawater with salinity 35 g kg^{-1} (typical of the oceans) as a function of temperature are combined to form the viscous length scale $R_\mu \equiv \mu^2/\rho\gamma$. This length scale is plotted along with an Arrhenius fit of the form $R_\mu(T) = A\exp\left(\frac{B}{C+T/^\circ\text{C}}\right)$, where $A = 62.02$ nm, $B = 661.3$, and $C = 100.1$. The Arrhenius fit differs from the combined reference correlations by less than 0.5% for the whole temperature range $0\,^\circ\text{C} \leq T \leq 40\,^\circ\text{C}$.

C (wt %)	T (°C)	ρ (kg m^{-3})	μ (mPa s)	γ (mN m^{-1})	R (µm)	La
0	23.2	997	0.931	72.0	35	2910
15	21.6	1037	1.43	70.0	23	814
30	23.5	1076	2.22	68.5	39	580
30	23.5	1076	2.22	68.5	30	449
50	23.0	1129	5.37	67.4	33	87
0	23.0	997	0.933	72.0	213	17500
20	24.8	1050	1.52	69.5	208	6530
30	24.1	1076	2.18	68.5	206	3200
35	25.1	1089	2.56	68.2	204	2310
40	25.3	1102	3.20	67.9	203	1480
45	25.3	1116	3.89	67.7	202	1010
47.5	23.2	1122	4.90	67.5	202	636
50	22.6	1129	5.55	67.4	201	496
55	23.3	1142	6.94	67.2	200	318
60	23.6	1155	9.35	66.9	199	176

TABLE I. Fluid properties and bubble size for microfluidic and micropipette experiments. C is the glycerol concentration (weight percent) of the solution, T is the lab temperature, R is the bubble size, and La is the corresponding Laplace number. Densities and surface tensions of glycerol-water solutions are obtained from reference values [49], while viscosities are measured with a viscometer for the micropipette experiments and given by an empirical formula [50] taking into account temperature variations for the microfluidic experiments.

Temperature (°C)	Density (kg m^{-3})	Viscosity (mPa s)	Surface tension (mN m^{-1})	R_μ (nm)
0	1028.0	1.906	76.64	46.1
8	1027.2	1.479	75.54	28.2
10	1027.0	1.397	75.26	25.2
20	1024.9	1.077	73.81	15.3
30	1022.0	0.861	72.31	10.0
40	1018.3	0.707	70.74	6.95

TABLE II. Seawater properties as a function of temperature for a salinity of 35 g kg^{-1} [45, 46]. The viscous length scale $R_\mu \equiv \mu^2/\rho\gamma$ is included as well.

[1] C. Textor, M. Schulz, S. Guibert, S. Kinne, Y. Balkanski, S. Bauer, T. Berntsen, T. Berglen, O. Boucher, M. Chin, et al. Analysis and quantification of the diversities of aerosol life cycles within aerocom. *Atmos. Chem. Phys.*, 6(7):1777–1813, 2006.

[2] E. R. Lewis and S. E. Schwartz. *Sea Salt Aerosol Production: Mechanisms, Methods, Measurements, and Models—A Critical Review*. American Geophysical Union, 2004.

[3] D. C. Blanchard and L. Syzdek. Mechanism for the water-to-air transfer and concentration of bacteria. *Science*, 170(3958):626–628, 1970.

[4] E. Baylor, M. Baylor, D. C. Blanchard, L. D. Syzdek, and C. Appel. Virus transfer from surf to wind. *Science*, 198(4317):575–580, 1977.

[5] Y. S. Joung, Z. Ge, and C. R. Buie. Bioaerosol generation by raindrops on soil. *Nat. Commun.*, 8, 2017.

[6] L. T. Angenent, S. T. Kelley, A. S. Amand, N. R. Pace, and M. T. Hernandez. Molecular identification of potential pathogens in water and air of a hospital therapy pool. *Proc. Natl. Acad. Sci. U.S.A.*, 102(13):4860–4865, 2005.

[7] D. Johnson, R. Lynch, C. Marshall, K. Mead, and D. Hirst. Aerosol generation by modern flush toilets. *Aerosol Sci. Technol.*, 47(9):1047–1057, 2013.

[8] J. Gralton, E. Tovey, M.-L. McLaws, and W. D. Rawlinson. The role of particle size in aerosolised pathogen transmission: a review. *J. Infect.*, 62(1):1–13, 2011.

[9] S. G. Boyce. The salt spray community. *Ecol. Monogr.*, 24(1):29–67, 1954.

[10] C. Kientzler, A. B. Arons, D. C. Blanchard, and A. H. Woodcock. Photographic investigation of the projection of droplets by bubbles bursting at a water surface. *Tellus*, 6(1):1–7, 1954.

[11] D. Moore and B. Mason. The concentration, size distribution and production rate of large salt nuclei over the oceans. *Quart. J. Roy. Meteor. Soc.*, 80(346):583–590, 1954.

[12] D. Newitt, N. Dombrowski, and F. Knelman. Liquid entrainment. 1. the mechanism of drop formation from gas or vapour bubbles. *Trans. Inst. Chem. Eng.*, 32:244–261, 1954.

[13] F. Garner, S. Ellis, and J. Lacey. The size distribution and entrainment of droplets. *Trans. Inst. Chem. Eng*, 32:222–235, 1954.

[14] D. Blanchard and A. Woodcock. Bubble formation and modification in the sea and its meteorological significance. *Tellus*, 9(2):145–158, 1957.

[15] D. C. Blanchard. The electrification of the atmosphere by particles from bubbles in the sea. *Prog. Oceanogr.*, 1:73–202, 1963.

[16] S. Hayami and Y. Toba. Drop production by bursting of air bubbles on the sea surface (1) experiments at still sea water surface. *J. Oceanogr. Soc. Jpn.*, 14(4):145–150, 1958.

[17] R. A. Medrow and B. Chao. Charges on jet drops produced by bursting bubbles. *J. Colloid Interface Sci.*, 35(4):683–688, 1971.

[18] R. Tedesco and D. Blanchard. Dynamics of small bubble motion and bursting in freshwater. *J. Rech. Atmos*, 13(3):215–226, 1979.

[19] M. Sakai. Ion distribution at a nonequilibrium gas/liquid interface. *J. Colloid Interface Sci.*, 127(1):156–166, 1989.

[20] D. E. Spiel. The number and size of jet drops produced by air bubbles bursting on a fresh water surface. *J. Geophys. Res. Oceans*, 99(C5):10289–10296, 1994.

[21] D. E. Spiel. The sizes of the jet drops produced by air bubbles bursting on sea-and fresh-water surfaces. *Tellus B*, 46(4):325–338, 1994.

[22] D. E. Spiel. More on the births of jet drops from bubbles bursting on seawater surfaces. *J. Geophys. Res. Oceans*, 102(C3):5815–5821, 1997.

[23] J. S. Lee, B. M. Weon, S. J. Park, J. H. Je, K. Fezzaa, and W.-K. Lee. Size limits the formation of liquid jets during bubble bursting. *Nat. Commun.*, 2:367, 2011.

[24] E. Ghabache and T. Séon. Size of the top jet drop produced by bubble bursting. *Phys. Rev. Fluids*, 1(5):051901, 2016.

[25] G. De Leeuw, E. L. Andreas, M. D. Anguelova, C. Fairall, E. R. Lewis, C. O'Dowd, M. Schulz, and S. E. Schwartz. Production flux of sea spray aerosol. *Reviews of Geophysics*, 49(2), 2011.

[26] X. Wang, G. B. Deane, K. A. Moore, O. S. Ryder, M. D. Stokes, C. M. Beall, D. B. Collins, M. V. Santander, S. M. Burrows, C. M. Sultana, et al. The role of jet and film drops in controlling the mixing

state of submicron sea spray aerosol particles. *Proc. Natl. Acad. Sci. U.S.A.*, page 201702420, 2017.

[27] L. Duchemin, S. Popinet, C. Josserand, and S. Zaleski. Jet formation in bubbles bursting at a free surface. *Phys. Fluids*, 14(9):3000–3008, 2002.

[28] A. M. Gañán-Calvo. Revision of bubble bursting: Universal scaling laws of top jet drop size and speed. *Phys. Rev. Lett.*, 119(20):204502, 2017.

[29] See supplemental material at [url] for movies of bubble formation in the microfluidic device and jet drop formation from experiments and numerical simulations.

[30] S.-C. Georgescu, J.-L. Achard, and É. Canot. Jet drops ejection in bursting gas bubble processes. *Eur. J. Mech. B*, 21(2):265–280, 2002.

[31] P. L. Walls, L. Henaux, and J. C. Bird. Jet drops from bursting bubbles: How gravity and viscosity couple to inhibit droplet production. *Phys. Rev. E*, 92(2):021002, 2015.

[32] S. Popinet. Gerris: a tree-based adaptive solver for the incompressible euler equations in complex geometries. *J. Comput. Phys.*, 190(2):572–600, 2003.

[33] S. Popinet. *The Gerris Flow Solver*, 2007. `http://gfs.sf.net`.

[34] S. Popinet. An accurate adaptive solver for surface-tension-driven interfacial flows. *J. Comput. Phys.*, 228(16):5838–5866, 2009.

[35] J. Hoepffner and G. Paré. Recoil of a liquid filament: escape from pinch-off through creation of a vortex ring. *J. Fluid Mech.*, 734:183, 2013.

[36] L. Deike, E. Ghabache, G. Liger-Belair, A. K. Das, S. Zaleski, S. Popinet, and T. Séon. Dynamics of jets produced by bursting bubbles. *Phys. Rev. Fluids*, 3:013603, 2018.

[37] E. Ghabache, A. Antkowiak, C. Josserand, and T. Séon. On the physics of fizziness: How bubble bursting controls droplets ejection. *Phys. Fluids*, 26(12):121701, 2014.

[38] T. Driessen, R. Jeurissen, H. Wijshoff, F. Toschi, and D. Lohse. Stability of viscous long liquid filaments. *Phys. Fluids*, 25(6):062109, 2013.

[39] B. W. Zeff, B. Kleber, J. Fineberg, and D. P. Lathrop. Singularity dynamics in curvature collapse and jet eruption on a fluid surface. *Nature*, 403(6768):401–404, 2000.

[40] D. Bartolo, C. Josserand, and D. Bonn. Singular jets and bubbles in drop impact. *Phys. Rev. Lett.*, 96(12):124501, 2006.

[41] S. Gekle and J. Gordillo. Generation and breakup of worthington jets after cavity collapse. part 1. jet formation. *J. Fluid Mech.*, 663:293–330, 2010.

[42] J. Gordillo and S. Gekle. Generation and breakup of worthington jets after cavity collapse. part 2. tip breakup of stretched jets. *J. Fluid Mech.*, 663:331–346, 2010.

[43] Y. Toba. Drop production by bursting of air bubbles on the sea surface (ii) theoretical study on the shape of floating bubbles. *J. Oceanogr. Soc. Jpn.*, 15(3):121–130, 1959.

[44] H. Princen. Shape of a fluid drop at a liquid-liquid interface. *J. Colloid Sci.*, 18(2):178–195, 1963.

[45] M. H. Sharqawy, J. H. Lienhard, and S. M. Zubair. Thermophysical properties of seawater: a review of existing correlations and data. *Desalin. Water Treat.*, 16(1-3):354–380, 2010.

[46] K. G. Nayar, M. H. Sharqawy, L. D. Banchik, et al. Thermophysical properties of seawater: a review and new correlations that include pressure dependence. *Desalination*, 390:1–24, 2016.

[47] D. K. Woolf, P. A. Bowyer, and E. C. Monahan. Discriminating between the film drops and jet drops produced by a simulated whitecap. *J. Geophys. Res. Oceans*, 92(C5):5142–5150, 1987.

[48] E. Mårtensson, E. Nilsson, G. de Leeuw, L. Cohen, and H.-C. Hansson. Laboratory simulations and parameterization of the primary marine aerosol production. *J. Geophys. Res. Atmos.*, 108(D9), 2003.

[49] W. M. Haynes. *CRC handbook of chemistry and physics*. CRC press, 2014.

[50] N.-S. Cheng. Formula for the viscosity of a glycerol- water mixture. *Ind. Eng. Chem. Res.*, 47(9):3285–3288, 2008.